

Using coda wave interferometry for estimating the variation in source mechanism between double couple events

D. J. Robinson,^{1,2} R. Snieder,³ and M. Sambridge¹

Received 2 January 2007; revised 12 August 2007; accepted 29 August 2007; published 12 December 2007.

[1] It is shown how a change in orientation between the source mechanism of two identically located double couple sources can be estimated from the correlation of the coda waves excited by their sources. The change in orientation is given by the root mean square of the change in strike, $\Delta\phi_s$, dip, $\Delta\delta$ and rake, $\Delta\lambda$ of the double couple. It is not possible to determine $\Delta\phi_s$, $\Delta\delta$ or $\Delta\lambda$ individually from the cross correlation. Applicability of the theory is tested using synthetic waveforms generated from a 3D finite difference solver for the elastic wave equation. Changes in strike, dip and rake are tested independently and simultaneously. In each case a crossover point is identified such that the actual change in orientation is within one standard deviation of the coda wave interferometry (CWI) estimates for all rotations below the crossover. After the crossover, the CWI estimates give a lower bound on the change in orientation. Crossover points of 30°, 62°, and 56°, respectively are observed when the strike, dip and rake are varied independently. When all angles are varied simultaneously by the same quantity the crossover point is 17°. The new theory can be applied in combination with existing coda wave interferometry techniques for estimating source separation. It creates the potential for joint relative location and focal mechanism determination using information from seismic coda recorded at a single station.

Citation: Robinson, D. J., R. Snieder, and M. Sambridge (2007), Using coda wave interferometry for estimating the variation in source mechanism between double couple events, *J. Geophys. Res.*, 112, B12302, doi:10.1029/2007JB004925.

1. Introduction

1.1. Modeling Earthquake Mechanisms

[2] Understanding the physics of seismic sources is important for many applications in seismology. Modeling earthquake mechanisms provided seismological support for theories on plate tectonics [Isacks *et al.*, 1968] and seafloor growth [Sykes, 1967]. Mechanisms are regularly used at regional [e.g., Dreger and Helmberger, 1993; Zhao and Helmberger, 1994] and local [e.g., Thurber *et al.*, 2006; Hardebeck, 2006] distances to interpret seismicity and understand earthquake processes. They are routinely derived for globally recorded earthquakes by the Global Centroid Moment Tensor (CMT) project [Dziewonski *et al.*, 1981; Dziewonski and Woodhouse, 1983; Ekström *et al.*, 1998].

[3] An earthquake mechanism can be approximated by a point source when its dimension, L is small compared to the wavelengths, λ of interest [Jost and Herrmann, 1989]. Stein and Wysession [2003] derive this criterion by first demon-

strating that the difference in arrival time between waves traveling from different ends of a fault is given by T_R , the total rupture time for the fault. Secondly, they argue that the dominant period, T must be larger than T_R , otherwise the waveform will be significantly affected by waves radiating from different parts of the source. Finally, Stein and Wysession [2003] show that

$$\frac{T_R}{T} = \frac{L}{\lambda}, \quad (1)$$

hence demonstrating that a point source approximation is adequate when the source dimension is small compared to the wavelength. Similarly, we can impose the criterion that the dominant frequency of the waveforms is smaller than the corner frequency f_c (or the circular corner frequency ω_c) since for simple models of the source spectra $\frac{1}{T_R} = f_c$ [e.g., Brune, 1970; Scholz, 2004].

[4] There are two widely used descriptions for the point source mechanism [Kennett, 1988]. Both approaches represent the source by a set of equivalent body forces. The classical description includes a fault plane, on which slip occurs, and its perpendicular auxiliary plane. This formulation is restricted to explaining shear dislocation or double-couple sources. A more versatile description of the seismic point-source is given by the moment tensor. Moment tensors can describe seismic sources that lead to volumetric

¹Research School of Earth Sciences, Australian National University, Canberra, ACT, Australia.

²Risk Research Group, Geoscience Australia, Canberra, ACT, Australia.

³Center for Wave Phenomena and Department of Geophysics, Colorado School of Mines, Golden, Colorado, USA.

change as well as composite linear vector dipoles and double-couples. We use the notation of the moment tensor, but our analysis is restricted to double-couple sources.

[5] Techniques for modeling the mechanism of a point-source can be broadly separated into two categories. The first category exploits the polarity and/or amplitude of P- and S- waves directly, whereas the second category considers the pulse shape of the arriving wave through waveform matching. The simplest of the polarity/amplitude based techniques uses the first motion (P wave) polarity to identify locations on a source centered sphere that initially undergo compression and dilatation. For a double couple, this approach divides the sphere into four quadrants that represent the focal mechanism. Examples of its use are given by Sykes [1967] and Oppenheimer *et al.* [1988]. Hardebeck and Shearer [2002] and Kilb and Hardebeck [2006] describe how the accuracy of first motion polarity techniques can be improved if uncertainties in the event location, velocity model and polarity are considered during the inversion for focal mechanism or fault plane solution.

[6] The use of S-wave information can improve the stability of mechanism inversion. Herrmann [1975] and Nakamura [2002] describe how to use both P and S-wave polarities simultaneously; and Kisslinger [1980], Kisslinger *et al.* [1981], Julian and Foulger [1996] and Hardebeck and Shearer [2003] discuss the inclusion of S/P wave amplitude ratios. Snoko [2003] provides a software package FOCMEC, that incorporates P and S wave polarities as well as S/P wave amplitude ratios in the inversion for source mechanism.

[7] Waveform techniques involve comparing sections of the observed waveforms with those derived synthetically using idealized models. Typically the process is couched in an inversion routine whereby earthquake parameters are sought to satisfy a pre-defined misfit criteria when synthetic and observed waveforms are compared. A number of approaches have been developed. These differ in the way they treat the observations (e.g., filtering, truncation); generate the synthetic waveforms (e.g., frequency wave number (F-K) integration, superposition of normal modes); the manner in which they describe the source (e.g., moment tensor or double couple focal mechanism); and the parameters that vary during the inversion (e.g., source mechanism, event location, velocity model). The nature of these choices influences the applicability of the technique.

[8] For example, Dziewonski *et al.* [1981] describe a technique for simultaneously modeling earthquake mechanisms and hypocenter location from teleseismic waveforms. The waveforms are truncated and filtered ($T > 45$ s) to focus on long-period body waves and hence reduce uncertainties associated with small scale variations in the velocity model. The superposition of normal modes is used to generate synthetics. An extension of this approach is provided by Dziewonski and Woodhouse [1983] who include the use of longer-period surface waves known as mantle waves ($T > 135$ s) for events with $M_w > 6$. Collectively, these two procedures are used to determine the moment tensor solutions for the Global Centroid Moment Tensors (CMT) project. Originally, surface waves with period $T < 135$ s were ignored in the CMT approach because they are particularly sensitive to lateral variations in Earth structure [Dziewonski *et al.*, 1981], details of which were not captured in available velocity models. However, Arvidsson and

Ekström [1998] and Ekström *et al.* [1998] provide a further enhancement to the CMT technique which includes surface waves with $40 \text{ s} < T < 60 \text{ s}$ by incorporating new 3D mantle-[Ekström and Dziewonski, 1995] and global phase-[Ekström *et al.*, 1997] velocity maps.

[9] Sipkin [1994] describes an alternative approach for determining moment tensors from teleseismically recorded P waveform data. By focussing on P waves only it is possible to obtain moment tensor estimates of most earthquakes with magnitude 5.8 or greater within 20 min of data arrival at a central location. Another variation for teleseismic mechanism determination is given by Marson-Pidgeon *et al.* [2000] and Kennett *et al.* [2000] who use nonlinear inversion and SV- waveforms to combine the hypocenter and mechanism determination from a limited number of short-period teleseismic records. The ability of the latter-technique to work with less stations facilitates its use with lower magnitude events which may not be recorded as widely.

[10] Dreger and Helmberger [1993] model source parameters from sparsely distributed three-component regional recordings. Their technique also requires filtering and truncation of the waveforms so that only long-period body waves are considered. It simultaneously solves for both mechanism and location. It has been successfully applied in Turkey for earthquakes with $M_w \geq 3.7$ [Örgülü *et al.*, 2003] and automated in California for real time moment tensor solutions [Pasyanos *et al.*, 1996]. In the latter case Rayleigh waves are also incorporated. There are other examples describing the simultaneous use of long-period body and surface waves at regional distances [e.g., Langston, 1981; Randall *et al.*, 1995]. All of these regional waveform matching techniques use Green's functions derived from one dimensional (layered) velocity models to generate the synthetics. This is usually required due to inadequate knowledge of the 3D structure. The approach is successful because of the restriction to long-period waves which are less sensitive to lateral velocity variations than are their short period counterparts [Langston, 1981; Dreger and Helmberger, 1993; Pasyanos *et al.*, 1996]. Zhao and Helmberger [1994] demonstrate how separating the seismogram into smaller sub-sections combined with the use of L1 and L2 norms (to emphasize different properties) facilitates the use of regional broadband waveforms (i.e., containing high frequencies) without adversely effecting the determined mechanism. The success of this technique required the simultaneous use of polarity information as well as waveform matching.

[11] Typically, the interpretation of small to moderate sized local earthquake mechanisms has focused on P- and S-wave polarity and P/S-wave amplitude studies. However, attempts at using waveform data in local settings have been made by some authors. Saikia and Hermann [1985] combine polarity and amplitude techniques with waveform matching of short sections centered on the P- and S- wave arrivals. Restriction to these arrivals permits the use of high frequency (up to 10 Hz) data with a 1D velocity model. A similar approach is taken by Shomali and Slunga [2000], who also use a 1D velocity model and small sections of the high frequency (1 to 4 Hz or 1 to 6 Hz) waveform around the P- and S-wave arrivals.

[12] Jost *et al.* [2002] and Ramos-Martínez and McMechan [2001] use the search method of Zhao and Helmberger

[1994] to model focal mechanisms of local earthquakes. Recall that this technique was originally applied to regional data. *Jost et al.* [2002] consider earthquakes with $-0.2 < M_l < 2.2$ in the Aegean area, Europe. The technique produced focal mechanisms that did not compare favorably with those derived from polarity and amplitude information. Differences may be associated with erroneous first motion data or inadequacy of the employed 1D velocity model to explain the 3D structure [*Jost et al.*, 2002]. That is, at local scales the waveforms are more sensitive to heterogeneity at the frequencies of interest compared to the original regional application of *Zhao and Helmberger* [1994]. *Ramos-Martínez and McMechan* [2001] demonstrate that combining the search techniques of *Zhao and Helmberger* [1994] with a detailed 3D velocity model can lead to the successful interpretation of local earthquakes. This is illustrated by comparing focal mechanisms derived from local recordings with those from regional recordings of 2 Northridge 1994 earthquake aftershocks. *Ramos-Martínez and McMechan* [2001] also demonstrate by means of a synthetic study that a reduction in waveform residuals of $\approx 50\%$ can be obtained when the 3D velocity structure of the San Fernando basin is considered rather than the 1D layered model for the region. The remaining residual is associated with vertical crack anisotropy ($\approx 30\%$) and attenuation ($\approx 20\%$). Despite its success with Northridge aftershocks, the use of the *Zhao and Helmberger* [1994] technique for local events is limited because detailed 3D velocity models are rarely available.

[13] In this paper we examine constraints on the source mechanism from coda waves. Theory is presented that relates the change in orientation between two source mechanisms and the cross correlation of their coda waves. Applicability of the theory is tested numerically.

1.2. Earthquake Properties From Coda Waves

[14] The latter arriving waves on a seismogram arise from scattering and are known as coda waves [*Aki*, 1969; *Snieder*, 1999; *Snieder*, 2006]. Some authors have used coda to infer properties of the source and/or media [e.g., *Aki*, 1969; *Aki and Chouet*, 1975; *Abubakirov and Gusev*, 1990; *Margerin et al.*, 1999]. In a seminal paper, *Aki* [1969] adopted a statistical treatment to describe the generation of coda in terms of single-backscattering waves and used it to compute the seismic moment from the coda of local earthquakes. *Aki and Chouet* [1975] introduce an alternative explanation for the generation of coda via a diffusion process. They discuss links between source spectra, attenuation and coda using single-backscattering and diffusion theories for coda wave generation. More recent explanations of coda generation consider multiple scattering, an interpolation between the two extremes [*Hoshiba*, 1991; *Margerin et al.*, 2000]. An emerging use of coda waves, known as coda wave interferometry (CWI), is based on the interference pattern between the coda of two events [*Snieder and Vrijlandt*, 2005; *Snieder*, 2006]. This idea has been used to determine seismic velocity changes in laboratory specimens [*Roberts et al.*, 1992; *Snieder et al.*, 2002; *Grêt et al.*, 2006], volcanoes [*Ratdomopurbo and Poupinet*, 1995; *Grêt et al.*, 2005] and fault zones [*Poupinet et al.*, 1984]. Despite these examples, the majority of seismological applications discard the coda.

[15] *Snieder and Vrijlandt* [2005] demonstrated the use of CWI to estimate the separation in spatial position between two earthquakes with assumed comparable source mechanism (geometry of the fault plane, slip vector) and source spectrum over the employed frequencies. The later requirement is attained by considering waveforms with frequencies smaller than the corner frequency of each event. Changes in the source mechanism between the events also influences the cross correlation and therefore contaminate CWI estimates of source separation. In this paper we derive the theory for relating the change in orientation of two identically located double couple source mechanisms to the cross correlation computed from their waveforms. The relationship is remarkably simple and, unlike the CWI source separation estimates, is not dependent on the frequency content of the waveforms.

[16] To test the new theory we use a 3D elastic wave solver to synthetically generate waveforms from gradually perturbed source mechanisms. By comparing the known source mechanism changes with estimates from the theory we are able to validate the derived relationship for small changes in orientation.

2. Theory

[17] The normalized time-shifted cross correlation is given by

$$R^{(t,t_w)}(t_s) = \frac{\int_{t-t_w}^{t+t_w} u_i(t') \tilde{u}_i(t' + t_s) dt'}{\left(\int_{t-t_w}^{t+t_w} u_i^2(t') dt' \int_{t-t_w}^{t+t_w} \tilde{u}_i^2(t') dt' \right)^{\frac{1}{2}}}, \quad (2)$$

where t_s is the shift time. It measures the change between the reference u_i and perturbed \tilde{u}_i displacement in the direction i over a time window of length $2t_w$ [*Snieder and Vrijlandt*, 2005]. The displacement terms in equation (2) can be replaced with velocity or acceleration, provided the same wavefield is used for both events. Note that $R^{(t,t_w)}(0)$ is the correlation coefficient. *Snieder* [2006] demonstrates how the maximum of the normalised cross correlation over the time window t_w is related to the variance of the traveltime perturbation σ_τ by

$$R_{\max}^{(t,t_w)} = 1 - \frac{1}{2} \overline{\omega^2} \sigma_\tau^2, \quad (3)$$

where the mean square of the angular frequency $\overline{\omega^2}$ is given by

$$\overline{\omega^2} = \frac{\int_{t-t_w}^{t+t_w} \dot{u}_i^2(t') dt'}{\int_{t-t_w}^{t+t_w} u_i^2(t') dt'}, \quad (4)$$

and \dot{u}_i represents the derivative of u_i with respect to time, t . In this paper the derivative $\dot{u}(t)$ is computed by numerical differentiation of $u(t)$. The relationship between the source separation D and σ_τ is given by

$$D^2 = g(\alpha, \beta) \sigma_\tau^2. \quad (5)$$

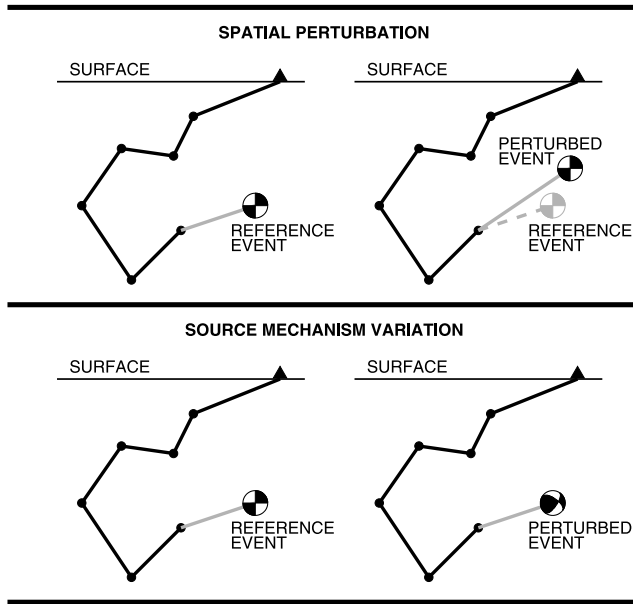


Figure 1. Application of coda wave interferometry (CWI) to source displacement (top) and source variation (bottom). The first segment of each travel path is illustrated in grey and depicts travel between the event (focal mechanism) and the first scatterer (circle). The remainder of the travel path (black line) indicates reflections from multiple scatterers before reaching the recording station (triangle). In the source displacement case the event is moved spatially without change to the mechanism whereas in the new theory, the orientation of the mechanism is changed without variation in location. In the former differences in the recorded waveforms result from a traveltime perturbation associated with variation in the first segment of the path. In the latter case the waveforms differ due to a change in radiation pattern associated with the change in orientation.

[18] Here α and β refer to P- and S-wave velocities, respectively and the source separation D is a scalar quantity containing no information about direction. The function g depends on the type of excitation (explosion, point force, double couple) and on the direction of the source displacement relative to the point force or double couple. For example, *Snieder and Vrijlandt* [2005] demonstrate that for two double couple sources displaced in the fault plane

$$g(\alpha, \beta) = 7 \frac{\left(\frac{2}{\alpha^6} + \frac{3}{\beta^6}\right)}{\left(\frac{6}{\alpha^8} + \frac{7}{\beta^8}\right)}. \quad (6)$$

2.1. Formulation of the CWI Source Mechanism Problem

[19] Using a similar approach, we derive a relationship between the variation in source orientation of two double couple events and the cross correlation of their coda. Consider two events with different focal mechanisms located at the same hypocenter. Ignoring variation in magnitude between the events, the waveforms that leave the source

in a particular direction differ in amplitude due to a change in radiation pattern associated with the variation in source orientation. There is no traveltime delay for waves that follow the same scattering path due to the identical location. This point is the fundamental difference between the derivation described here and that of *Snieder and Vrijlandt* [2005] for CWI applied to estimating source separation. In their treatment the change in spatial position creates a traveltime delay (or advance). A comparison of the two CWI approaches is given in Figure 1.

[20] In the following we consider waves excited by a double couple source. For convenience we refer to one of the sources as the reference event and the second as the varied event. This nomenclature recognizes that the varied mechanism is attained by changing the dip, rake and strike of the reference event. The particle displacement (shown by the seismogram) associated with the reference event at an arbitrary station can be computed by summing the displacement from all scattering trajectories, T that reach the station

$$u_i(t) = A_m \sum_T u_i^{(T)}(t), \quad (7)$$

where $u_i^{(T)}$ is the component of displacement from scattering path T in direction i normalized by A_m , the amplitude of event with magnitude, m . The sum over all trajectories, T also represents a sum over wave types, P wave and the two S wave polarizations, for each path segment. The perturbed wave at the same station can be written as

$$\tilde{u}_i(t) = \tilde{A}_m \sum_T \tilde{u}_i^{(T)}(t) = \tilde{A}_m \sum_T (1 + r^{(T)}) u_i^{(T)}(t), \quad (8)$$

where $\tilde{u}_i^{(T)}$ is the component of displacement from scattering path T in the i th direction normalized by \tilde{A}_m and $r^{(T)}$ measures the change in waves radiated by the source along scattering path T . In the presence of strong scattering the ‘normalized energy’ in the perturbed and reference waves is the same. That is,

$$\int \sum_T u_i^{(T)2}(t') dt' = \int \sum_T (1 + r^{(T)})^2 u_i^{(T)2}(t) dt', \quad (9)$$

where the integrals are taken over the entire length of the coda. For small changes in source orientation and sufficiently large time windows $2t_w$, the following approximation holds

$$\int_{t-t_w}^{t+t_w} \sum_T u_i^{(T)2}(t') dt' \approx \int_{t-t_w}^{t+t_w} \sum_T (1 + r^{(T)})^2 u_i^{(T)2}(t) dt'. \quad (10)$$

[21] The size of the time window required for a given level of accuracy depends on the change in orientation between the sources. The accuracy of equation (10) can be determined directly from the waveforms. The maximum cross correlation occurs when $t_s = 0$ because there is no traveltime delay (or advance) associated with a source mechanism change.

[22] When equations (7), (8), and (10) are inserted into the cross-correlation we get a double sum $\sum_{T \neq T'}^T$ which can be decomposed into diagonal- and cross-terms $\sum_{T \neq T'}^T = \sum_{T=T'}^T + \sum_{T \neq T'}^T$. In coda wave interferometry the cross terms $\sum_{T \neq T'}^T$ lead to fluctuations in the correlation function that characterizes the change. These fluctuations are reduced as the window length, $2t_w$ is increased [Snieder, 2004]. In coda wave interferometry the cross-terms are ignored to simplify the derivation of key results [Snieder, 2006].

[23] Substituting $t_s = 0$ and equations (7), (8), and (10) into equation (2) leads to

$$R_{\max}^{(t, t_w)} = 1 + \langle r \rangle, \quad (11)$$

where

$$\langle r \rangle = \frac{\sum_T r^{(T)} \int_{t-t_w}^{t+t_w} u_i^{(T)2}(t') dt'}{\sum_T \int_{t-t_w}^{t+t_w} u_i^{(T)2}(t') dt'} \quad (12)$$

is the path-weighted average of the change in displacement. Note that $\langle r \rangle$ can be computed directly from the perturbed and reference waveforms.

2.2. Relating $\langle r \rangle$ to the Variation in Source Mechanism

[24] The displacement, $u_i^{(T)}$ can be re-written as

$$u_i^{(T)} = \dot{s}(t - t^{(T)}) f^{(T)} A^{(T)} p_i^{(T)}, \quad (13)$$

where $\dot{s}(t - t^{(T)})$ is the source time function derivative with time, $t^{(T)}$ is the traveltime along trajectory T , $f^{(T)}$ is the amplitude of radiation taking off along trajectory T , $A^{(T)}$ is the product of geometrical spreading and scattering coefficients and $p_i^{(T)}$ is the i component of the polarization vector that we assume to be measured for waves propagating along T . Assuming that $s(t)$, $p_i^{(T)}$ and $A^{(T)}$ are identical for the events we can re-write equation (12) as

$$\langle r \rangle = \frac{\sum_T r^{(T)} f^{(T)2} p_i^{(T)2} \int_{t-t_w}^{t+t_w} s^2(t' - t^{(T)}) dt'}{\sum_T f^{(T)2} p_i^{(T)2} \int_{t-t_w}^{t+t_w} s^2(t' - t^{(T)}) dt'} = \frac{\sum_T r^{(T)} f^{(T)2}}{\sum_T f^{(T)2}}, \quad (14)$$

and, using

$$\tilde{u}_i^{(T)}(t) = (1 + r^{(T)}) u_i^{(T)}(t), \quad (15)$$

we obtain

$$r^{(T)} = \frac{\tilde{f}^{(T)}}{f^{(T)}} - 1, \quad (16)$$

where $\tilde{f}^{(T)}$ is the radiation term for the perturbed event. For elastic wave propagation we separate the radiation term, $f^{(T)}$ into P, SH and SV waves as follows

$$f^{(T)} = f^{(T,P)} + f^{(T,SV)} + f^{(T,SH)}, \quad (17)$$

hence

$$\langle r \rangle = \frac{\sum_T r^{(T,P)} f^{(T,P)2} + \sum_T r^{(T,SH)} f^{(T,SH)2} + \sum_T r^{(T,SV)} f^{(T,SV)2}}{\sum_T f^{(T,P)2} + \sum_T f^{(T,SH)2} + \sum_T f^{(T,SV)2}}, \quad (18)$$

where the, P, SH and SV denote the wave type as it leaves the source. Replacing the summation over all paths with an angular integration over all takeoff angles yields

$$\langle r \rangle = \frac{\int (r^{(T,P)} f^{(T,P)2} + r^{(T,SH)} f^{(T,SH)2} + r^{(T,SV)} f^{(T,SV)2}) d\Omega}{\int f^{(T,P)2} d\Omega + \int f^{(T,SH)2} d\Omega + \int f^{(T,SV)2} d\Omega} \quad (19)$$

where $d\Omega = \sin\theta d\theta d\phi$, and the integration limits for $d\theta$ and $d\phi$ are $[0, 2\pi]$ and $[0, \pi]$, respectively.

[25] We let

$$M_{jk} = M_{jk}(\phi_s, \lambda, \delta) \quad (20)$$

represent the moment tensor of the reference event where ϕ_s , λ , δ indicate the strike, rake and dip, respectively. The moment tensor in polar coordinates is related to these angles by

$$\begin{aligned} M_{11} &= -M_o (\sin \delta \cos \lambda \sin 2\phi_s + \sin 2\delta \sin \lambda \sin^2 \phi_s) \\ M_{12} &= M_{21} = -M_o \left(\sin \delta \cos \lambda \cos 2\phi_s + \frac{1}{2} \sin 2\delta \sin \lambda \sin 2\phi_s \right) \\ M_{13} &= M_{31} = -M_o (\cos \delta \cos \lambda \cos \phi_s + \cos 2\delta \sin \lambda \sin \phi_s) \\ M_{22} &= M_o (\sin \delta \cos \lambda \sin 2\phi_s - \sin 2\delta \sin \lambda \cos^2 \phi_s) \\ M_{23} &= M_{32} = M_o (\cos \delta \cos \lambda \sin \phi_s - \cos 2\delta \sin \lambda \cos \phi_s) \\ M_{33} &= M_o \sin 2\delta \sin \lambda, \end{aligned} \quad (21)$$

where M_o represents the scalar moment [Kennett, 1988; Kennett, 2001; Pujol, 2003]. The moment tensor of the perturbed event is given by $\tilde{M}_{jk} = \tilde{M}_{jk}(\phi_s + \Delta\phi_s, \lambda + \Delta\lambda, \delta + \Delta\delta)$, where $\Delta\phi_s$, $\Delta\lambda$ and $\Delta\delta$ represent the change in strike, rake and dip, respectively. For small changes in these angles \tilde{M}_{jk} can be approximated with a Taylor Series expansion

$$\begin{aligned} \tilde{M}_{jk} &= M_{jk} + \Delta\phi_s \frac{\partial M_{jk}}{\partial \phi_s} + \Delta\lambda \frac{\partial M_{jk}}{\partial \lambda} + \Delta\delta \frac{\partial M_{jk}}{\partial \delta} + \frac{\Delta\phi_s^2}{2} \frac{\partial^2 M_{jk}}{\partial \phi_s^2} \\ &+ \frac{\Delta\lambda^2}{2} \frac{\partial^2 M_{jk}}{\partial \lambda^2} + \frac{\Delta\delta^2}{2} \frac{\partial^2 M_{jk}}{\partial \delta^2} + \Delta\phi_s \Delta\lambda \frac{\partial^2 M_{jk}}{\partial \phi_s \partial \lambda} \\ &+ \Delta\phi_s \Delta\delta \frac{\partial^2 M_{jk}}{\partial \phi_s \partial \delta} + \Delta\lambda \Delta\delta \frac{\partial^2 M_{jk}}{\partial \lambda \partial \delta} + O(|\Delta_{\text{angle}}|^3). \end{aligned} \quad (22)$$

[26] From the far field approximations for the P, SV and SH displacements [e.g., *Pujol*, 2003], and equation (13), we obtain

$$f^{(P)} = \frac{1}{4\pi\rho\alpha^3} \hat{\mathbf{r}} \mathbf{M} \hat{\mathbf{r}}^T, \quad (23)$$

$$f^{(SH)} = \frac{1}{4\pi\rho\beta^3} \hat{\boldsymbol{\theta}} \mathbf{M} \hat{\boldsymbol{\theta}}^T, \quad (24)$$

and

$$f^{(SH)} = \frac{1}{4\pi\rho\beta^3} \hat{\boldsymbol{\phi}} \mathbf{M} \hat{\boldsymbol{\phi}}^T, \quad (25)$$

where ρ is the density. The unit vectors $\hat{\mathbf{r}}$, $\hat{\boldsymbol{\theta}}$ and $\hat{\boldsymbol{\phi}}$ are given by $(\sin \theta \cos \phi, \sin \theta \sin \phi, \cos \theta)$, $(\cos \theta \cos \phi, \cos \theta \sin \phi, -\sin \theta)$ and $(-\sin \phi, -\cos \phi, 0)$, respectively. Using equations (23) to (25) and integrating equation (17) over all take off angles gives

$$\int f^{(T)2} d\Omega = \frac{1}{4\pi\rho r} \left(\frac{16\pi}{15\alpha^6} M_o^2 + \frac{24\pi}{15\beta^6} M_o^2 \right). \quad (26)$$

[27] To derive a relationship between the change in orientation between the two source mechanisms and the path-weighted average of the change in amplitude we consider a specific example. We use a coordinate system with the x - z plane aligned with the fault plane and the x axis in the direction of the identically oriented strike and slip vectors. In that coordinate system $\delta = \pi/2$, $\lambda = 0$, $\phi_s = 0$ and equation (21) gives a moment tensor of form

$$M = \begin{pmatrix} 0 & -M_o & 0 \\ -M_o & 0 & 0 \\ 0 & 0 & 0 \end{pmatrix}. \quad (27)$$

[28] The choice of these parameters for the source is made to simplify the derivation. However, the relationship that follows is applicable to any starting focal mechanism due to the angular integration in equation (19).

[29] First, we consider the P waves. The P wave contribution for scattering path T is given by equation (23). The P wave contribution for the same scattering path of the perturbed wave is given by

$$\begin{aligned} \tilde{f}^{(T,P)} = & \frac{1}{4\pi\rho\alpha^3} \left(\hat{\mathbf{r}} \mathbf{M} \hat{\mathbf{r}}^T + \Delta\phi_s \hat{\mathbf{r}} \frac{\partial \mathbf{M}}{\partial \phi_s} \hat{\mathbf{r}}^T + \Delta\lambda \hat{\mathbf{r}} \frac{\partial \mathbf{M}}{\partial \lambda} \hat{\mathbf{r}}^T \right. \\ & \cdot \Delta\delta \hat{\mathbf{r}} \frac{\partial \mathbf{M}}{\partial \delta} \hat{\mathbf{r}}^T + \frac{\Delta\phi_s^2}{2} \hat{\mathbf{r}} \frac{\partial^2 \mathbf{M}}{\partial \phi_s^2} \hat{\mathbf{r}}^T + \frac{\Delta\lambda^2}{2} \hat{\mathbf{r}} \frac{\partial^2 \mathbf{M}}{\partial \lambda^2} \hat{\mathbf{r}}^T \\ & + \frac{\Delta\delta^2}{2} \hat{\mathbf{r}} \frac{\partial^2 \mathbf{M}}{\partial \delta^2} \hat{\mathbf{r}}^T + \Delta\phi_s \Delta\lambda \hat{\mathbf{r}} \frac{\partial^2 \mathbf{M}}{\partial \phi_s \partial \lambda} \hat{\mathbf{r}}^T \\ & \left. + \Delta\phi_s \Delta\delta \hat{\mathbf{r}} \frac{\partial^2 \mathbf{M}}{\partial \phi_s \partial \delta} \hat{\mathbf{r}}^T + \Delta\lambda \Delta\delta \hat{\mathbf{r}} \frac{\partial^2 \mathbf{M}}{\partial \lambda \partial \delta} \hat{\mathbf{r}}^T \right) \hat{r}_i. \end{aligned} \quad (28)$$

[30] Combining equations (23) and (28) with equation (16) leads to $r^{(T,P)}$, the change in P wave displacement along scattering path T

$$\begin{aligned} r^{(T,P)} = & \Delta\phi_s \left(\frac{2 \sin^2 \theta \cos 2\phi}{\sin^2 \theta \sin 2\phi} \right) + \Delta\lambda \left(\frac{-\sin 2\theta \sin \phi}{\sin^2 \theta \sin 2\phi} \right) \\ & + \Delta\delta \left(\frac{-\sin 2\theta \cos \phi}{\sin^2 \theta \sin 2\phi} \right) - \frac{1}{2} (4\Delta\phi_s^2 + \Delta\lambda^2 + \Delta\delta^2) \\ & + \Delta\phi_s \Delta\lambda \left(\frac{-\sin 2\theta \cos \phi}{\sin^2 \theta \sin 2\phi} \right) + \Delta\phi_s \Delta\delta \left(\frac{\sin 2\theta \sin \phi}{\sin^2 \theta \sin 2\phi} \right) \\ & + \Delta\lambda \Delta\delta \left(\frac{2 \cos^2 \theta - \sin^2 \theta \sin^2 \phi}{\sin^2 \theta \sin 2\phi} \right). \end{aligned} \quad (29)$$

[31] Using equations (23) and (29) and integrating over the takeoff angles gives

$$\int r^{(T,P)} f^{(T,P)2} d\Omega = \frac{1}{4\pi\rho r} \frac{-8\pi M_o^2}{15\alpha^6} (\Delta\delta^2 + 4\Delta\phi_s^2 + \Delta\lambda^2). \quad (30)$$

[32] We repeat the same treatment in the Appendix for the SV- and SH-waves and obtain

$$\int r^{(T,SV)} f^{(T,SV)2} d\Omega = \frac{1}{4\pi\rho r} \frac{-2\pi M_o^2}{15\beta^6} (\Delta\delta^2 + 4\Delta\phi_s^2 + \Delta\lambda^2), \quad (31)$$

and

$$\int r^{(T,SH)} f^{(T,SH)2} d\Omega = \frac{1}{4\pi\rho r} \frac{-2\pi M_o^2}{3\beta^6} (\Delta\delta^2 + 4\Delta\phi_s^2 + \Delta\lambda^2), \quad (32)$$

respectively.

[33] Combining equations (26), (30), (31) and (32) with equation (19) gives the simple expression

$$\langle r \rangle = -\frac{1}{2} (\Delta\delta^2 + 4\Delta\phi_s^2 + \Delta\lambda^2). \quad (33)$$

[34] The relationship between the cross correlation and the change in source mechanism, measured by the root mean square change in source parameters, is given by combining equations (11) and (33)

$$R_{\max}^{(t,t_w)} = 1 - \frac{1}{2} (\Delta\delta^2 + 4\Delta\phi_s^2 + \Delta\lambda^2). \quad (34)$$

[35] The use of non-overlapping windows to compute $R_{\max}^{(t,t_w)}$ provides independent estimates of $\langle r \rangle$ for different center times t . These can be used to check consistency, or for error analysis. *Snieder* [2004] shows that the relative contribution of cross terms, ignored in this derivation, is of order $\sqrt{1/\Delta F 2t_w}$ where $2t_w$ is the sliding window length and Δf is the bandwidth of the signal. A large window

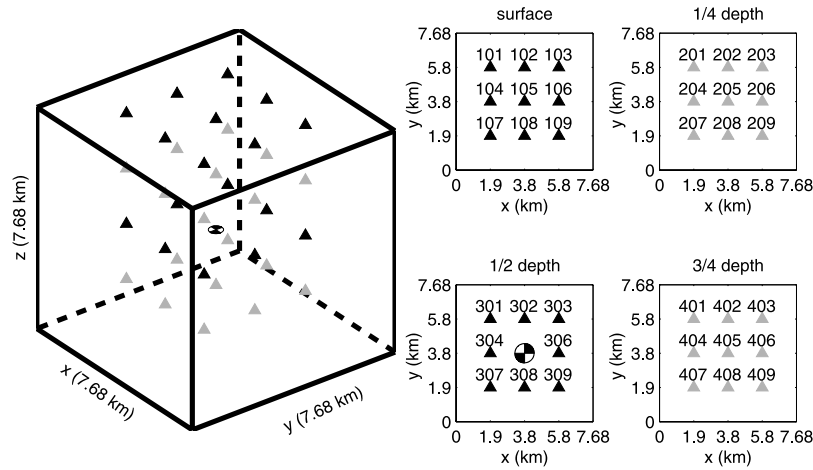


Figure 2. Configuration of the model domain in 3D (left). The reference source is indicated by a focal mechanism. The 35 recording stations (triangles) are shown for the surface (black), second (grey), third (black) and bottom (grey) depth levels in 3D on the left and in 2D slices on the right.

length reduces the fluctuations due to cross terms at the expense of having fewer independent estimates.

[36] Equation (34) relates the variation in mechanism between two double couples directly from the cross correlation of their coda. It demonstrates the possibility of combining coda wave and first motion techniques for relative focal mechanism determination. Alternatively, there

is scope for a combined application of this theory with CWI estimates of source separation to create a joint relative location and focal mechanism determination.

3. Numerical Validation

[37] In order to understand the range of applicability for equation (34), we use a finite difference (FD) solver of the

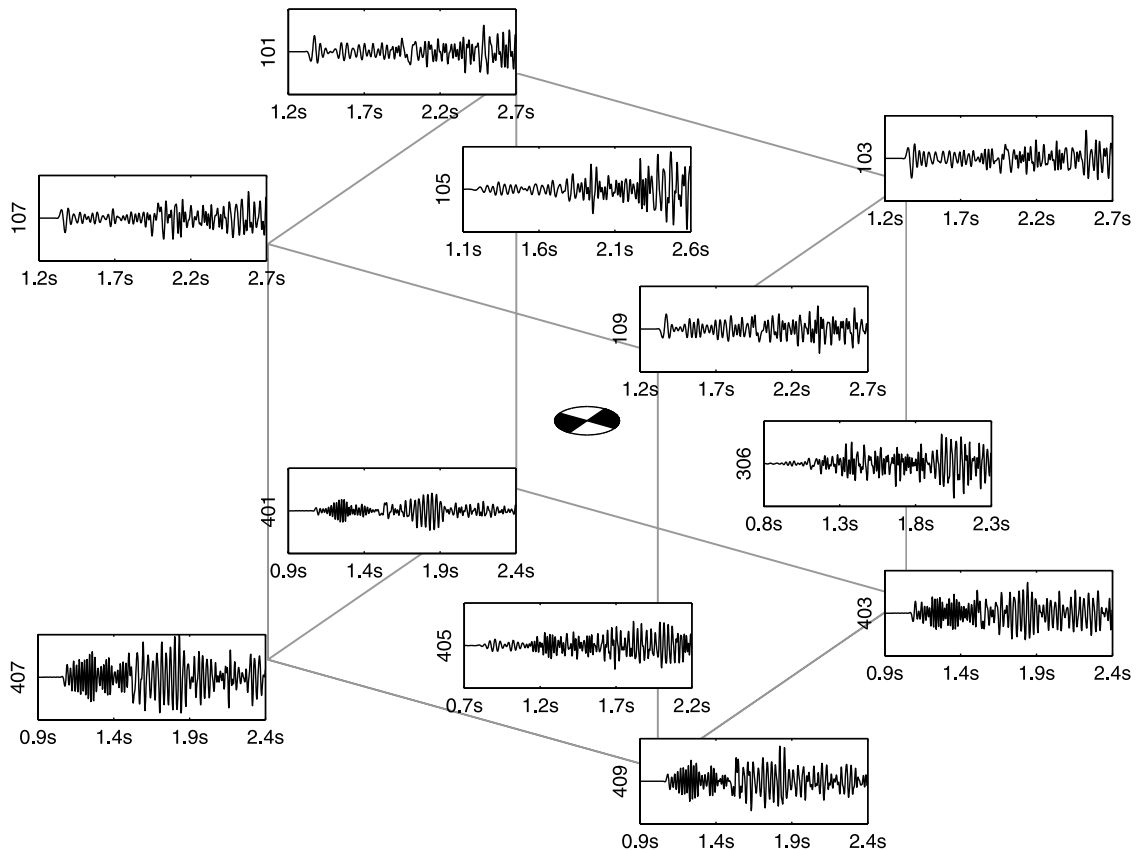


Figure 3. Initial 1.5 s sections of vertical component reference waveforms for 5 stations at the surface (101,103,105,107,109) and bottom (401, 403, 405, 407, 409) and one station in the plane of the event (306). Station location is depicted in Figure 2.

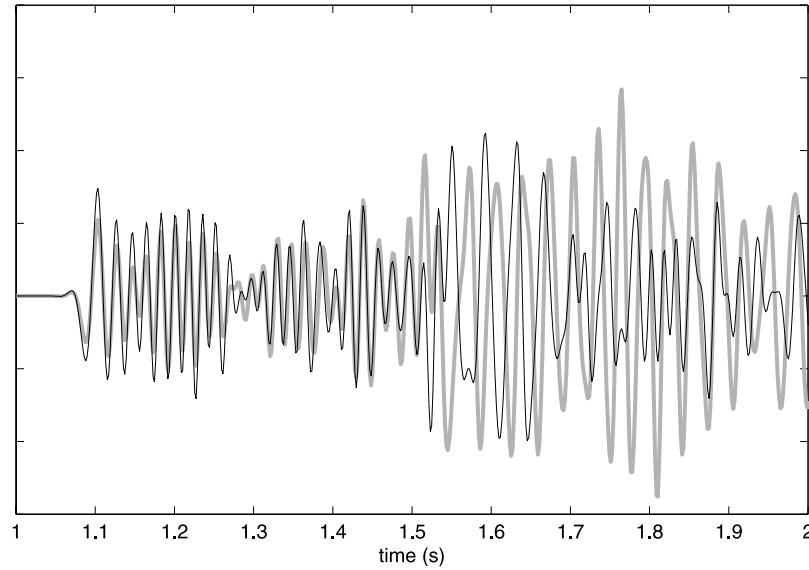


Figure 4. One second section comparing the reference waveform (thin-black) recorded in the horizontal y-channel of station 203 with that modeled after a change in strike of 24° (thick-grey).

3D elastic wave equation to generate waveforms for testing the CWI source variation theory. The FD solver PMLCL3D, supplied by Kim Olsen, is used on a Beowulf cluster. The solver implements a staggered-grid velocity-stress finite difference scheme with fourth order accuracy in space and second order accuracy in time [Olsen, 1994; Graves, 1996; Olsen *et al.*, 2006]. The model domain extends 7.68 km in each of the three dimensions. To alleviate reflections from the boundaries PMCL3D implements perfectly matched absorbing (PML) boundary conditions [Collino and Tsogka, 2001; Marcinkovich and Olsen, 2003] on the sides and bottom boundary. The surface is modeled by a second-order technique which places the vertical velocity component and the xz and xy stress components precisely on the surface (i.e., the FS2 approach of Gottschämer and Olsen, 2001).

[38] The P wave velocity, α of the medium is represented by a 3D Gaussian random medium with mean P wave velocity $\mu_\alpha = 5000 \text{ ms}^{-1}$, velocity perturbation of 4% (i.e., standard deviation $\sigma_\alpha = 200 \text{ ms}^{-1}$) and correlation length of 150 m. The S wave velocity is defined by

$$\beta = \frac{\alpha}{1.65}, \quad (35)$$

the density set to 2600 kgm^{-3} everywhere and the grid point separation 40 m. In the derivation of equation (34) we assumed that coda recorded at a given station arises from waves leaving the source in all directions. To achieve this, the scattering must be sufficiently strong; a requirement which is attained by the chosen velocity.

[39] The reference source is located in the center of the model domain. It is defined by a double couple with strike $\phi_s = 0$, dip $\delta_d = 90$, rake $\lambda = 0$ and scalar seismic moment $M_o = 1$. The source time function is created using a Gaussian pulse of form

$$s(t) = \exp\left(\frac{-(t - 0.42)^2}{2\tau^2}\right), \quad (36)$$

with $\tau = 0.01 \text{ s}$.

[40] Figure 2 illustrates the 35 recording stations distributed over four depth levels. The top level is located at the free-surface and the second, third and fourth levels are at depths of 1/4 (or 1.92 km), 1/2 (3.84 km), and 3/4 (5.76 km) of the model domain, respectively. Each station records waveforms in 3 channels corresponding to motion in the vertical and two horizontal directions. The vertical component waveforms are shown in Figure 3 for 5 stations in layers 1 (stations 101, 103, 107, 109, and 105) and 4 (401, 403, 405, 407, 409) and for one station in the horizontal plane of the source (306). As expected from a vertically oriented strike-slip double couple, the vertical first arrivals at the free-surface (layer 1) illustrate compression in diag-

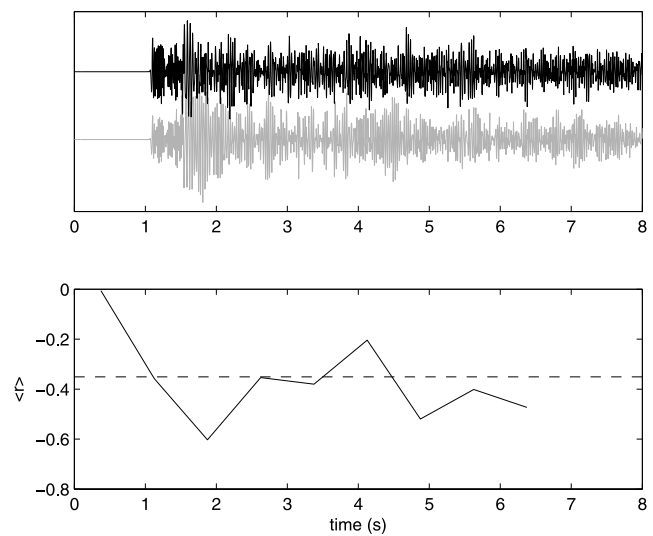


Figure 5. Comparison of reference waveform with the waveform after changing the strike by 24° . The top panel depicts the complete reference (black) and perturbed (grey) waveforms. The bottom panel illustrates the computed $\langle r \rangle$ as a function of sliding window of length 0.75 s.

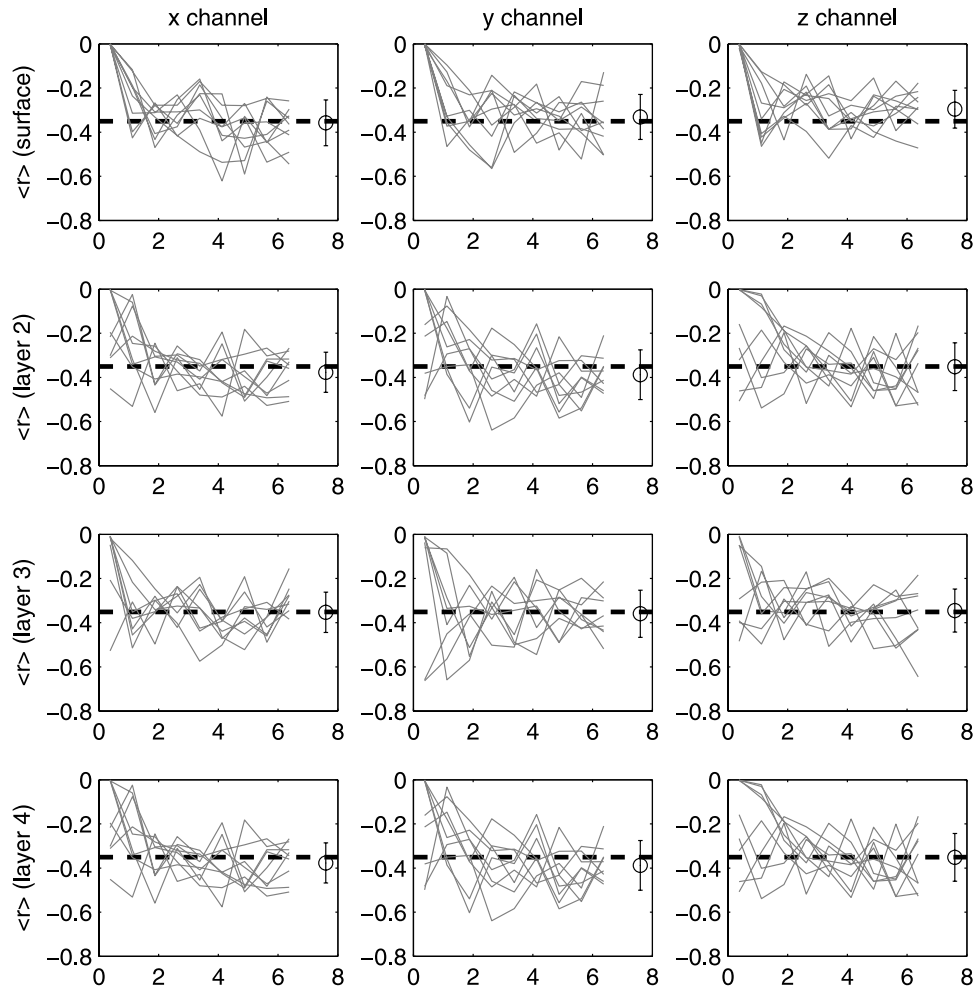


Figure 6. Computed $\langle r \rangle$ values illustrated as a function of sliding window for all channels. They are categorized into x, y, and z channel (columns) and layer (rows). The fluctuation about the known $\langle r \rangle$ (dashed lines) indicates that the theory is applicable for all channels in any direction from the source. Error bars at the end of each subplot indicate the mean (circle) and $\pm\sigma$ (tails) obtained after grouping the third through to the last sliding window estimates from each trace in the subplot. The first two sliding window estimates are ignored to ensure that S-wave coda is included in all windows. The dominance of S-waves in the coda have been discussed by several authors [e.g., Aki, 1992; Snieder and Vrijlandt, 2005].

onally opposing stations 103 and 107 and dilatation in stations 106 and 109.

[41] The polarity of vertical first P wave motion in each corner of layer 4 is opposite to that observed in layer 1. That is, station 403 shows dilatation whereas station 103, located directly above 403, is in compression. In most practical applications the first arrival recorded at a surface station comes from waves that began propagating downward from the source and were brought to the surface via refraction. This explains why focal mechanisms are usually illustrated with a lower hemisphere projection. In Figure 3 the first arrivals at the surface station originate from the source as upward propagating waves because there is no gradient in the velocity field to generate refraction.

[42] The first arrivals at stations 105, 405, and 306 are not as easy to pick because these stations are aligned with the fault (105 and 405) and auxiliary (306) planes. Such arrivals are known as emergent arrivals and commonly occur when

the stations are located on or close to the auxiliary or fault planes [Stein and Wysession, 2004]. Emergent arrivals may also occur when signal-to-noise ratios are low or in the presence of heterogeneity. Typically, emergent arrivals are discarded when determining focal mechanisms from polarity and/or amplitude data. Note however that equation (34) is equally applicable to the coda of waves with emergent first arrivals. Moreover, traditional approaches to focal mechanism application require good azimuthal station coverage. This is not necessary when applying equation (34) because information from all take-off angles is incorporated within the angular integrations described in section 2.

[43] Figure 4 compares one second of the reference waveform with that obtained when the strike is varied by 24° . The waveforms shown are the horizontal y-component recorded at station 203. The source change is not sufficient to cause any major differences between the first arrivals. However, variation between the coda is clearly observable.

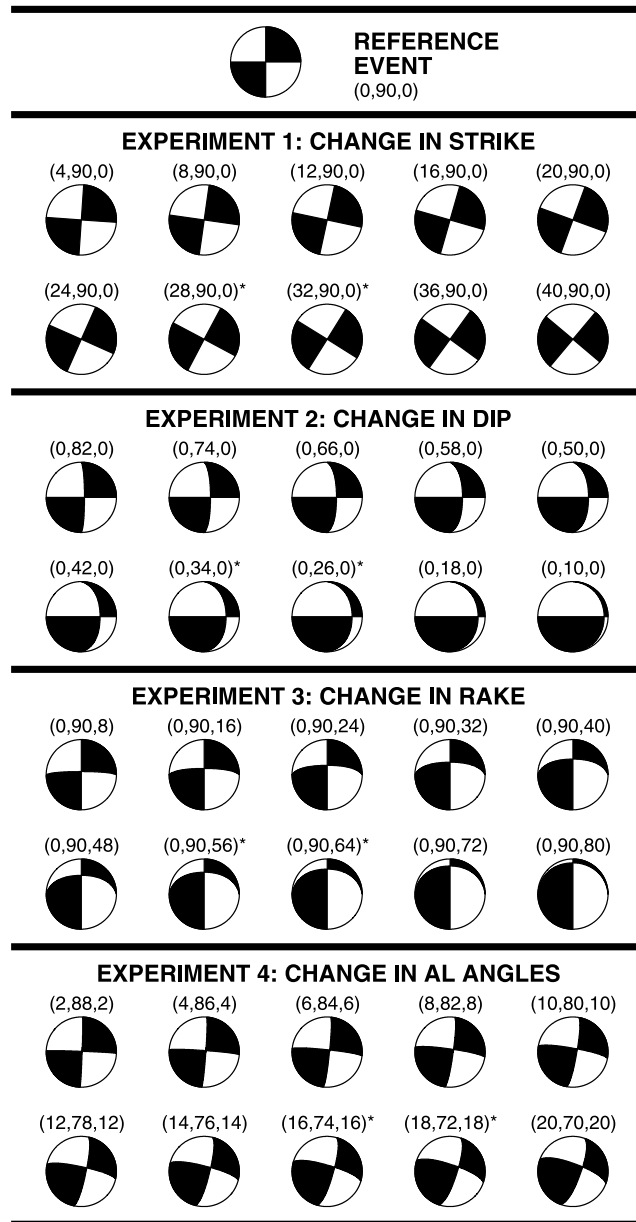


Figure 7. Range of focal mechanisms considered in the four experiments. The top row illustrates the reference event and the second row depicts a subset of the focal mechanisms used in experiment 1 which considers increasing strike in 2° increments from 2° to 40° . Row 3 illustrates focal mechanisms associated with experiment 2 (change in dip: 2° increments from 88° to 10°), row 4 depicts experiment 3 (change in rake: 2° increments from 2° to 80°) and row 5 illustrates experiment 4 (change in all three angles in 2° increments from 2° to 32°). Asterisks are used in each row to indicate the focal mechanisms between which the crossover point is found (see Figure 8). All focal mechanisms are lower hemisphere projections.

Apparent phase shifts between the reference and perturbed coda are not associated with traveltime delays along a specific trajectory. They arise due to differences in the superposition of amplitudes summed over all trajectories arriving at a given time.

[44] Figure 5 illustrates complete reference and perturbed waveforms for the same station-channel along with the computed $\langle r \rangle$ as a function of sliding window with width 0.75 s. The $\langle r \rangle$ fluctuates around the expected value of -0.35 (dashed line). Note that the cross-correlation is equal to $\langle r \rangle + 1$ (see equation (34)).

[45] Values of $\langle r \rangle$ inferred from the waveforms are shown as a function of sliding window for all channel-station combinations in Figure 6. For example, the top-left subplot illustrates computed $\langle r \rangle$ for the x-channel of all stations in layer at the surface. The observed fluctuations are related to the cross terms which are ignored in the derivation of equation (33) [Snieder, 2004]. It is because of these fluctuations that it is important to consider multiple non-overlapping time windows and, if available, waveforms from different stations. Error bars depicting the mean and standard deviation of all CWI estimates for a given layer-channel are shown at the end of each subplot. In the subsequent analysis the earliest two estimates are removed from each station before computing the errorbars because the early scattered waves do not have time to propagate in all directions from the source. This figure demonstrates that the known source change, measured by the root mean square of the change in source angles (equation (33)), is less than one standard deviation from the mean CWI estimate for waveforms recorded in all directions from the source. The result confirms that the theory is equally applicable for stations at any location. It suggests, as hypothesized in the theory, that data from a range of takeoff angles reach each station due to the scattering. Furthermore, the top row of Figure 6 suggests that surface-recorded waveforms provide sufficient information to estimate the source change.

[46] To explore the range in applicability of the theory we undertake four synthetic experiments. When describing different source mechanisms we indicate the strike, dip and rake in parenthesis as follows: (strike, dip, rake). For the reference event these angles are (0,90,0). In experiment 1 we consider the effect of 2° increases in strike from (2,90,0) to (40,90,0). A subset of the considered focal mechanisms are shown in row 2 of Figure 7. The reference focal mechanism is given in row 1 for comparison. The 105 waveforms for each perturbed mechanism are compared with the reference waveforms and equation (34) used to estimate the change in mechanism as a function of sliding window of length 0.75 s. This produces 9 estimates per channel or 945 estimates in total. Error bars are computed by combining all station-channel-window estimates (excluding the first two sliding window estimates from each cross correlation) and plotted in Figure 8a. That is, each error bar represents the distribution of 735 $\langle r \rangle$ estimates. As expected, the technique successfully estimates the change in mechanism for small variations. For large variations the technique provides a lower bound on the source change. It can not accurately determine the source change for large variations because of the Taylor series approximation in the theory which is less accurate for larger changes. In this case we observe that the CWI estimates are within one standard deviation of the known change in mechanism for all $\Delta\phi_s$ less than 30° . We refer to the point where the top of the errorbar $\mu + \sigma$, intersects the known separation as the crossover point.

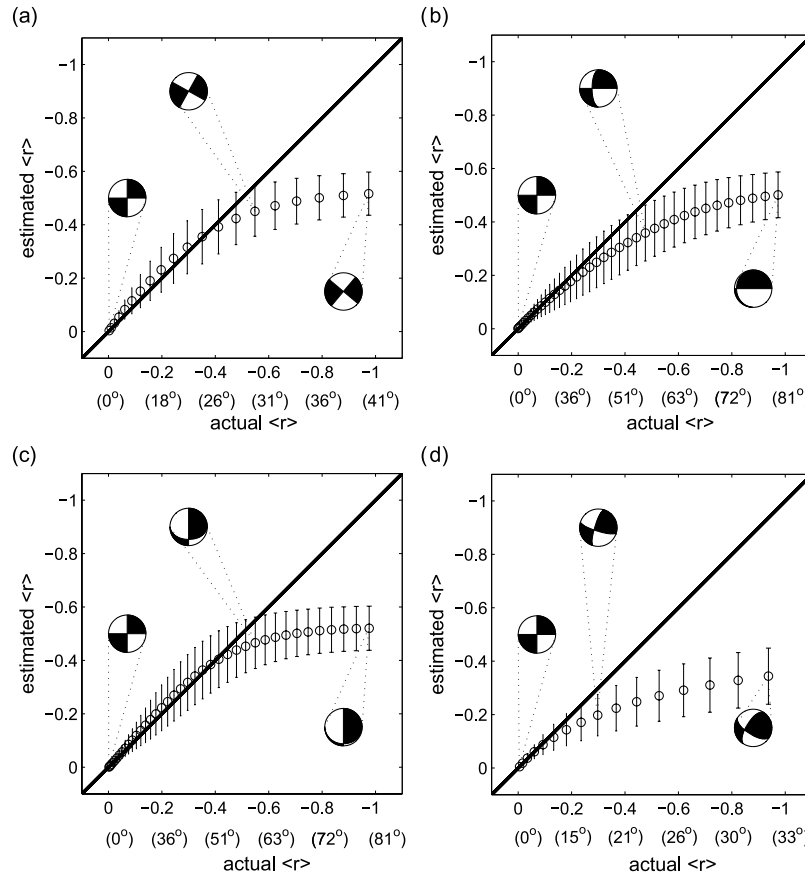


Figure 8. Errorbars depicting the range of applicability of equation (34) for variation in (a) strike $\Delta\phi_s$, (b) dip $\Delta\delta$, (c) rake $\Delta\lambda$, and (d) all three angles ($\Delta\phi_s$, $\Delta\delta$, $\Delta\lambda$) simultaneously. The solid diagonal line depicts values where the estimated and known $\langle r \rangle$ are identical. All four figures indicate a crossover point before which equation (34) provides accurate estimates of the known $\langle r \rangle$ and after which it provides a lower bound. Focal mechanisms are included to indicate the source variation associated with key points of each curve.

[47] In experiment 2 we consider variations of dip in 2° increments from (0,88,0) to (0,10,0). Associated variation in focal mechanisms are illustrated for a subset of those considered in row 3 of Figure 7. Repeating the analysis conducted for strike leads to 8(b). As with the strike experiments, we observe a crossover point before which the CWI estimates are accurate and after which they provide a lower bound on the known change. In this case the crossover point of $\Delta\delta = 62^\circ$ is roughly twice that observed with the strike. The factor of 2 arises from the square root of the coefficient 4 on $\Delta\phi_s^2$ when solving equation (34) for $\Delta\phi_s$.

[48] In experiment 3 we repeat the process for 2° increments in rake from (0,90,2) to (0,90,80) (see Figure 7 row 4 for illustrations). The errorbars of 8(c) indicate a crossover point of roughly 56° which is similar to that observed in experiment 2 for changes in dip. A comparison of Figures 8b and 8c indicates a subtle difference in curvature (as indicated by the error bar centers) between the rake and dip experiments.

[49] Finally, in experiment 4 we consider changes in all three mechanism angles simultaneously. In this case we consider concurrent increases (decreases for dip) in increments of 2° from (2,88,2) to (32, 58, 32) (see Figure 7 row 5). The resulting errorbars are displayed in 8(d). They

indicate a crossover point between 16° and 18° for simultaneous angle changes.

[50] The experiments are repeated twice; first with only the surface stations (9 stations with 189 $\langle r \rangle$ estimates) and secondly with only station 101 (21 $\langle r \rangle$ estimates). Figure 9 illustrates how the mean estimate $\mu_{\langle r \rangle}$ varies as a function of mechanism variation when all stations, those in the top (surface) layer and a single station are used for experiments 1 to 4 in subplots (a), (c), (e), and (f), respectively. These four subplots demonstrate that equation (34) leads to an accurate estimate of the mechanism variation (as given by $\mu_{\langle r \rangle}$) when either the surface stations or a single station are used in isolation. Subplots (b), (d), (e), and (h) illustrate how the standard deviation $\sigma_{\langle r \rangle}$ varies as a function of mechanism variation. The 21 $\langle r \rangle$ estimates provided by a single station lead to greater fluctuations in the $\sigma_{\langle r \rangle}$ curves than those observed when either the 9 surface or all 35 stations are used. However, the shape of the $\sigma_{\langle r \rangle}$ curves derived from a single station are similar to their counterparts that use either the surface data or that from all stations.

4. Discussion

[51] Source mechanisms can be computed from long-period regional and teleseismic waves using waveform

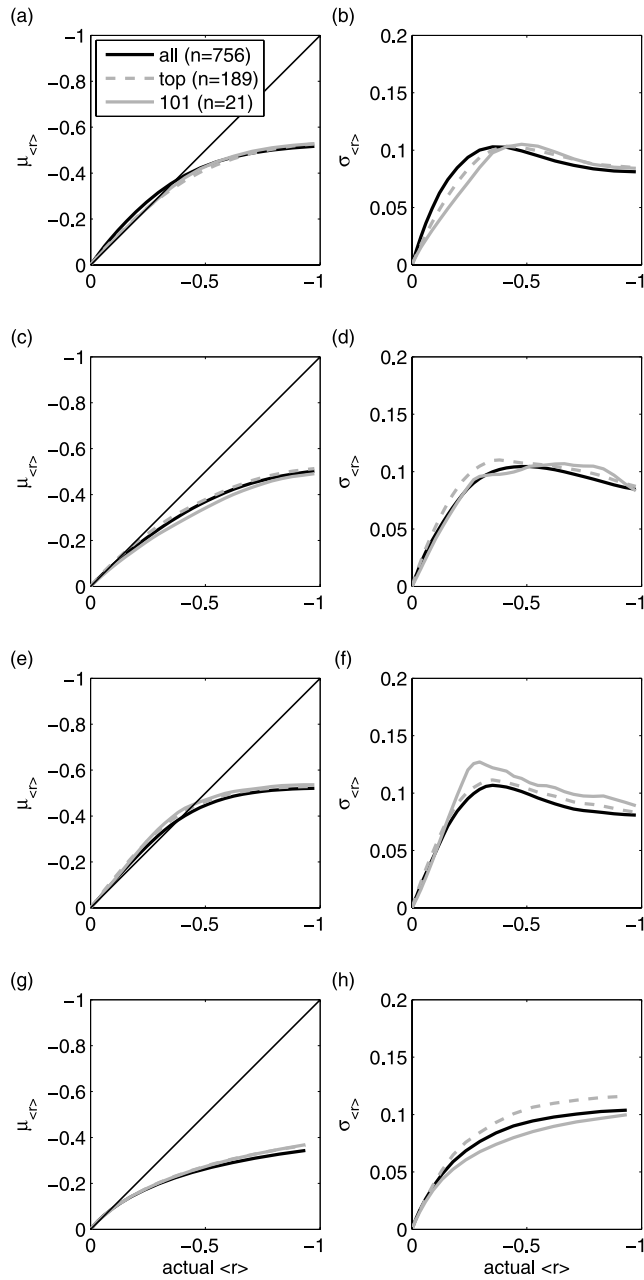


Figure 9. Mean $\mu_{\langle r \rangle}$ and standard deviation $\sigma_{\langle r \rangle}$ of the CWI estimates as a function of actual $\langle r \rangle$ when different stations are omitted. The results are plotted for the strike, dip, rake and multi experiments on rows 1 to 4, respectively. In each row $\mu_{\langle r \rangle}$ and $\sigma_{\langle r \rangle}$ are shown on the left and right, respectively. The subplots compare the statistics ($\mu_{\langle r \rangle}$ and $\sigma_{\langle r \rangle}$) when the CWI estimates are used from all stations (all), stations in the top layer (top) and station 101 (101).

matching techniques. At local distances the high frequency content is more important and the use of waveform techniques are less successful due to inaccuracies in the velocity model. One exception is given by *Ramos-Martínez and McMeahan* [2001] where a detailed 3D velocity model exists. For this reason most studies of local earthquakes model mechanisms using polarity and amplitude data. Such techniques are sensitive to poor azimuthal coverage, emer-

gent arrivals which are often discarded and incorrect station polarity. Moreover, erroneous polarity data can result from 3D structure that is not considered [*Oppenheimer et al.*, 1988]. The use of only polarity and amplitude data means that large sections of the recorded waveforms are not utilized.

[52] In this paper we develop a new theory which relates the correlation between coda of two double-couple events to the change in orientation between their source mechanism (as measured by the root mean square of the change in source angles). We consider events that have the same location and differ in mechanism only. Variations in magnitude and stress drop are also tolerable, provided the waveforms are filtered to a dominant frequency less than the corner frequency of both events. When this criterion is satisfied the source behaves effectively like a point source in time, and the slip history is a step function (as seen by the waves with frequency smaller than the corner frequency). However, if the dominant frequency exceeds the corner frequency the interference between waves radiated by different parts of the source must be accounted for.

[53] The theory is not sensitive to poor azimuthal coverage, emergent arrivals or incorrect station polarity. Furthermore, the method we present makes it possible to estimate the change in source orientation between events from coda waves recorded at a single station. The redundancy of multiple stations can be used as a consistency check, and to reduce the uncertainty in the estimated change in source angles. The technique can easily be automated when combined with a triggering algorithm to define the time interval in which coda waves arrive.

[54] Detailed knowledge of the velocity structure is also not required. The technique merely requires that the velocity structure is heterogeneous enough to support scattering and that the coda arriving at each station begins as waves propagating from the source in all directions. We do not directly account for first order discontinuities such as layering or the free surface. Such first order scattering produces wave reflections and conversions. We assume that non-planar scattering provides sufficient randomization of the directions of wave propagation and that the assumption that coda comprises waves from all take-off angles is not violated in the presence of first order discontinuities. The validity of this assumption is supported by Figures 6 and 9 which demonstrate that proximity of stations to the free surface does not adversely effect estimates of $\langle r \rangle$. Similarly, *Robinson et al.* [2007] demonstrate using synthetic experiments that there is no evident breakdown in the ability of CWI to estimate source separation as the depth of sources approach the free-surface. A further advantage of the CWI technique is that it incorporates high-frequency information from large sections of the waveform (i.e., the coda), a component that is typically discarded.

[55] In practice one would expect events to differ in both location and mechanism. Recall that the source separation formula (equation (3)) is dependent on frequency whereas the newly derived source variation one (equation (34)) is not. We propose that this difference in sensitivity to frequency can be exploited to identify both separation and source variation directly from the interference of coda waves. Therefore the theory presented in this paper

demonstrates the possibility of relative focal mechanism determination.

[56] Relative focal mechanism determination could be conducted for events with accurate locations by extracting only estimates of focal mechanism variation from the coda wave cross correlation. Alternatively, combining the separation and source variation branches of CWI facilitates a simultaneous relative location and mechanism determination. These coda wave techniques can be further combined with focal mechanism and location techniques that use phase arrival information for even more constraints.

[57] Such techniques will be useful whenever high precision location and mechanism information is desired. For example, one potential application involves estimating earthquake hazard from the transfer of stress associated with earthquakes. A brief overview of the relationship between stress and hazard is given by *Kilb and Hardebeck* [2006], who point out that this is a controversial area of research and that not all authors subscribe to the view that hazard can be estimated from changes in stress. Of those researching in this area, a number have demonstrated sensitivity of stress (hence hazard) estimates to accurate mechanism parameters [e.g., *Harris and Simpson*, 2002; *Kilb*, 2003]. *Abers and Gephart* [2001] also discuss the propagation of focal mechanism errors into stress modeling. In particular, they propose an inversion technique to compute stress directly from first motion data and therefore bypass the calculation of focal mechanisms and the need to incorporate a detailed error analysis. Actually, the focal mechanisms are simultaneously computed. *Abers and Gephart* [2001] demonstrate that even with 20–30 first motions having less than 5% polarity violations it is not possible to determine the stress orientation within a 20–30° error bound. Naturally, with less first motions one would expect the uncertainty on stress orientation to increase.

[58] In an application to local seismicity for three regions in California, *Hardebeck* [2006] undertakes a statistical analysis of differences in focal mechanisms for events at varying distances. *Hardebeck* [2006] demonstrates that the differences in mechanism, measured by the minimum single angular rotation, is typically less than the 1-sigma uncertainty of $\approx 25^\circ$ for events with separations less than 2 km. With such values of focal mechanism uncertainty it is not possible to distinguish whether computed differences in focal mechanism reflect actual differences or are merely a result of noise. It is in this range that the combined CWI technique we are proposing will be most sensitive. Therefore it potentially offers independent assessment on whether events in this distance range exhibit identical focal mechanisms.

5. Conclusion

[59] We present a new theory that relates the change in double couple mechanism between two identically located events and the cross correlation of their coda. Applicability of the theory is demonstrated using four synthetic experiments. In the first experiment we demonstrate that it is possible to estimate within one standard deviation, a change in strike of up to 30° directly from the cross correlation of coda. We refer to this point as the crossover point. For

angles exceeding 30° the CWI technique provides a lower bound for the change in orientation. Experiments varying the dip and rake indicate crossover points of 62° and 56° , respectively. In a fourth experiment we find a crossover point of 17° when all three double couple angles are varied simultaneously by the same quantity. Repeating the experiments with a single station demonstrates that the theory provides an accurate measure of source mechanism variation (as given by $\mu_{(r)}$) in the absence of complete azimuthal coverage. Sensitivity to mechanism variations in this range suggest that the theory may be applied in local settings as a further constraint to focal mechanism determination. The constraint can be applied via a relative focal mechanism determination approach which is analogous to the relative location techniques currently used in seismology.

Appendix A

[60] For the SV-wave along scattering path T we obtain

$$\begin{aligned} \tilde{f}^{(T,SV)} = \frac{1}{4\pi\rho\beta^3} & \left(\hat{\theta}\mathbf{M}\hat{\mathbf{r}}^T + \Delta\phi_s\hat{\theta}\frac{\partial\mathbf{M}}{\partial\phi_s}\hat{\mathbf{r}}^T + \Delta\lambda\hat{\theta}\frac{\partial\mathbf{M}}{\partial\lambda}\hat{\mathbf{r}}^T \right. \\ & + \Delta\delta\hat{\theta}\frac{\partial\mathbf{M}}{\partial\delta}\hat{\mathbf{r}}^T + \frac{\Delta\phi_s^2}{2}\hat{\theta}\frac{\partial^2\mathbf{M}}{\partial\phi_s^2}\hat{\mathbf{r}}^T + \frac{\Delta\lambda^2}{2}\hat{\theta}\frac{\partial^2\mathbf{M}}{\partial\lambda^2}\hat{\mathbf{r}}^T \\ & + \frac{\Delta\delta^2}{2}\hat{\theta}\frac{\partial^2\mathbf{M}}{\partial\delta^2}\hat{\mathbf{r}}^T + \Delta\phi_s\Delta\lambda\hat{\theta}\frac{\partial^2\mathbf{M}}{\partial\phi_s\partial\lambda}\hat{\mathbf{r}}^T \\ & \left. + \Delta\phi_s\Delta\delta\hat{\theta}\frac{\partial^2\mathbf{M}}{\partial\phi_s\partial\delta}\hat{\mathbf{r}}^T + \Delta\lambda\Delta\delta\hat{\theta}\frac{\partial^2\mathbf{M}}{\partial\lambda\partial\delta}\hat{\mathbf{r}}^T \right) \hat{\theta}_i, \end{aligned} \quad (\text{A1})$$

hence

$$\begin{aligned} r^{(T,SV)} = \Delta\phi_s & \left(\frac{2\sin 2\theta \cos 2\phi}{\sin 2\theta \sin 2\phi} \right) + \Delta\lambda \left(\frac{-\sin 2\phi \cos \theta}{\sin 2\theta \sin 2\phi} \right) \\ & + \Delta\delta \left(\frac{-2\cos \phi \cos 2\theta}{\sin^2 \theta \sin 2\phi} \right) - \frac{1}{2} (4\Delta\phi_s^2 + \Delta\lambda^2 + \Delta\delta^2) \\ & + \Delta\phi_s\Delta\lambda \left(\frac{-2\cos \phi \cos 2\theta}{\sin 2\theta \sin 2\phi} \right) + \Delta\phi_s\Delta\delta \left(\frac{2\sin 2\phi \cos 2\theta}{\sin 2\theta \sin 2\phi} \right) \\ & + \Delta\lambda\Delta\delta \left(\frac{-2\sin 2\theta (\sin^2 \phi + 1)}{\sin 2\theta \sin 2\phi} \right) \end{aligned} \quad (\text{A2})$$

and

$$\int r^{(T,SV)} f^{(T,SV)2} d\Omega = \frac{1}{4\pi\rho r} \frac{-2\pi M_o^2}{15\beta^6} (\Delta\delta^2 + 4\Delta\phi_s^2 + \Delta\lambda^2). \quad (\text{A3})$$

[61] Similarly, for the SH-wave on scattering path T we get

$$\begin{aligned} \tilde{f}^{(T,SH)} = \frac{1}{4\pi\rho\beta^3} & \left(\hat{\phi}\mathbf{M}\hat{\mathbf{r}}^T + \Delta\phi_s\hat{\phi}\frac{\partial\mathbf{M}}{\partial\phi_s}\hat{\mathbf{r}}^T + \Delta\lambda\hat{\phi}\frac{\partial\mathbf{M}}{\partial\lambda}\hat{\mathbf{r}}^T \right. \\ & + \Delta\delta\hat{\phi}\frac{\partial\mathbf{M}}{\partial\delta}\hat{\mathbf{r}}^T + \frac{\Delta\phi_s^2}{2}\hat{\phi}\frac{\partial^2\mathbf{M}}{\partial\phi_s^2}\hat{\mathbf{r}}^T + \frac{\Delta\lambda^2}{2}\hat{\phi}\frac{\partial^2\mathbf{M}}{\partial\lambda^2}\hat{\mathbf{r}}^T \\ & + \frac{\Delta\delta^2}{2}\hat{\phi}\frac{\partial^2\mathbf{M}}{\partial\delta^2}\hat{\mathbf{r}}^T + \Delta\phi_s\Delta\lambda\hat{\phi}\frac{\partial^2\mathbf{M}}{\partial\phi_s\partial\lambda}\hat{\mathbf{r}}^T \\ & \left. + \Delta\phi_s\Delta\delta\hat{\phi}\frac{\partial^2\mathbf{M}}{\partial\phi_s\partial\delta}\hat{\mathbf{r}}^T + \Delta\lambda\Delta\delta\hat{\phi}\frac{\partial^2\mathbf{M}}{\partial\lambda\partial\delta}\hat{\mathbf{r}}^T \right) \hat{\phi}_i, \end{aligned} \quad (\text{A4})$$

$$\begin{aligned}
r^{(T,SH)} = & \Delta\phi_s \left(\frac{-2 \sin \theta \sin 2\phi}{\sin \theta \cos 2\phi} \right) + \Delta\lambda \left(\frac{-\cos \phi \cos \theta}{\sin \theta \cos 2\phi} \right) \\
& + \Delta\delta \left(\frac{\sin \phi \cos \theta}{\sin \theta \cos 2\phi} \right) - \frac{1}{2} (4\Delta\phi_s^2 + \Delta\lambda^2 \Delta\delta^2) \\
& + \Delta\phi_s \Delta\lambda \left(\frac{\sin \phi \cos \theta}{\sin \theta \cos 2\phi} \right) + \Delta\phi_s \Delta\delta \left(\frac{\cos \phi \cos \theta}{\sin \theta \cos 2\phi} \right) \\
& + \Delta\lambda \Delta\delta \left(\frac{-\sin \theta \sin^2 \phi}{\sin \theta \cos 2\phi} \right) \quad (A5)
\end{aligned}$$

and

$$\int r^{(T,SH)} f^{(T,SH)2} d\Omega = \frac{1}{4\pi\rho r} \frac{-2\pi M_o^2}{3\beta^6} (\Delta\delta^2 + 4\Delta\phi_s^2 + \Delta\lambda^2). \quad (A6)$$

[62] **Acknowledgments.** The theory described in this manuscript was derived when one of us (DR) visited the Center for Wave Phenomena (CWP) at the Colorado School of Mines. The numerical validation was performed on the Terrawulf linux cluster at the Center for Advanced Data Inference, Research School of Earth Science. Peter Rickwood is thanked for his assistance with computations. Kim Olsen is acknowledged for providing the 3D finite difference solver for the elastic wave equation (pmc3d), and for advice on its use. The manuscript has been improved courtesy of reviews by Spiro Spiliopoulos and Trevor Dhu of Geoscience Australia, an anonymous reviewer and the JGR editorial team. Geoscience Australia is thanked for providing financial support.

References

- Abers, G. A., and J. W. Gephart (2001), Direct inversion of earthquake first motions for both the stress tensor and focal mechanisms and application to Southern California, *J. Geophys. Res.*, **106**(B11), 26,523–26,540.
- Abubakirov, I. R., and A. A. Gusev (1990), Estimation of scattering properties of lithosphere of Kamchatka based on Monte-Carlo simulation of record envelope of a near earthquake, *Phys. Earth Planet. Inter.*, **64**, 52–67.
- Aki, K. (1969), Analysis of the seismic coda of local earthquakes as scattered waves, *J. Geophys. Res.*, **74**(2), 615–631.
- Aki, K. (1992), Scattering conversions from P to S versus S to P, *Bull. Seismol. Soc. Am.*, **82**, 1969–1972.
- Aki, K., and B. Chouet (1975), Origin of coda waves: Source, attenuation, and scattering effects, *J. Geophys. Res.*, **80**(23), 3322–3342.
- Arvidsson, R., and G. Ekström (1998), Global CMT analysis of moderate earthquakes, $M_w \geq 4.5$, using intermediate-period surface waves, *Bull. Seismol. Soc. Am.*, **88**(4), 1003–1013.
- Brune, J. N. (1970), Tectonic stress and the spectra of seismic shearwaves from earthquakes, *J. Geophys. Res.*, **75**(26), 4997–5009.
- Collino, F., and C. Tsogka (2001), Application of the perfectly matched absorbing layer model to the linear elastodynamic problem in anisotropic heterogeneous media, *Geophysics*, **66**(1), 294–307.
- Dreger, D. S., and D. V. Helmberger (1993), Determination of source parameters at regional distances with three-component sparse network data, *J. Geophys. Res.*, **98**(B5), 8107–8125.
- Dziewonski, A. M., and J. H. Woodhouse (1983), An experiment in systematic study of global seismicity: Centroid-moment tensor solutions for 201 moderate and large earthquakes of 1981, *J. Geophys. Res.*, **88**(B4), 3247–3271.
- Dziewonski, A. M., T.-A. Chou, and J. H. Woodhouse (1981), Determination of earthquake source parameters from waveform data for studies of global and regional seismicity, *J. Geophys. Res.*, **86**(B4), 2825–2852.
- Ekström, G., and A. M. Dziewonski (1995), Improved models of upper mantle S velocity structure, *EOS*, **76**, F421.
- Ekström, G., G. J. Tromp, and E. W. Larson (1997), Measurements and global models of surface wave propagation, *J. Geophys. Res.*, **102**, 8137–8157.
- Ekström, G., A. Morelli, E. Boschi, and A. M. Dziewonski (1998), Moment tensor analysis of the central Italy earthquake sequence of September–October 1997, *Geophys. Res. Lett.*, **25**(11), 1971–1974.
- Gottschämer, E., and K. B. Olsen (2001), Accuracy of the explicit planar free–surface boundary condition implemented in a fourth–order staggered–grid velocity–stress finite–difference scheme, *Bull. Seismol. Soc. Am.*, **91**(3), 617–623.
- Graves, R. W. (1996), Simulating seismic wave propagation in 3D elastic media using staggered-grid finite differences, *Bull. Seismol. Soc. Am.*, **86**(4), 1091–1106.
- Grêt, A., R. Snieder, R. C. Aster, and P. R. Kyle (2005), Monitoring rapid temporal change in a volcano with coda wave interferometry, *Geophys. Res. Lett.*, **32**, L06304, doi:10.1029/2004GL021143.
- Grêt, A., R. Snieder, and J. Scales (2006), Time-lapse monitoring of rock properties with coda wave interferometry, *J. Geophys. Res.*, **111**, B03305, doi:10.1029/2004JB003354.
- Hardebeck, J. L. (2006), Homogeneity of small-scale earthquake faulting, stress, and fault strength, *Bull. Seismol. Soc. Am.*, **96**(5), 1675–1688, doi:10.1785/0120050257.
- Hardebeck, J. L., and P. M. Shearer (2002), A new method for determining first-motion focal mechanisms, *Bull. Seismol. Soc. Am.*, **92**(6), 2264–2276.
- Hardebeck, J. L., and P. M. Shearer (2003), Using S/P amplitude ratios to constrain the focal mechanisms of small earthquakes, *Bull. Seismol. Soc. Am.*, **93**(6), 2434–2444.
- Harris, R. A., and R. W. Simpson (2002), The 1999 M_w 7.1 Hector Mine, California, earthquake: A test of the stress shadow hypothesis, *Bull. Seismol. Soc. Am.*, **92**(4), 1497–1512.
- Herrmann, R. B. (1975), A student's guide to the use of P and S wave data for focal mechanism determination, *Earthquake Notes*, **46**(4), 29–39.
- Hoshiba, M. (1991), Simulation of multiple-scattered coda wave excitation based on the energy conservation law, *Phys. Earth Planet. Inter.*, **67**, 123–136.
- Isacks, B., J. Oliver, and L. R. Sykes (1968), Seismology and the new global tectonics, *J. Geophys. Res.*, **73**(18), 5855–5899.
- Jost, M. L., and R. B. Herrmann (1989), A student's guide to and review of moment tensors, *Seismol. Res. Lett.*, **60**(2), 37–57.
- Jost, M. L., O. Knabenbauer, J. Cheng, and H.-P. Harjes (2002), Fault plane solutions of microearthquakes and small events in the Hellenic arc, *Tectonophysics*, **356**, 87–114.
- Julian, B. R., and G. R. Foulger (1996), Earthquake mechanisms from linear-programming inversion of seismic-wave amplitude ratios, *Bull. Seismol. Soc. Am.*, **86**(4), 972–980.
- Kennett, B. L. N. (1988), Radiation from a moment-tensor source, in *Seismological Algorithms: Computational methods and computer programs*, edited by D. J. Doornbos, pp. 427–442, Academic Press.
- Kennett, B. (2001), *The seismic wavefield: Volume 1: Introduction and theoretical developments*, Cambridge Univ. Press, UK.
- Kennett, B., K. Marson-Pidgeon, and M. S. Sambridge (2000), Seismic source characterization using a neighbourhood algorithm, *Geophys. Res. Lett.*, **27**(20), 3401–3404.
- Kilb, D. (2003), A strong correlation between induced peak dynamic Coulomb stress change from the 1992 M7.3 Landers, California, earthquake and the hypocenter of the 1999 M7.1 Hector Mine, California, earthquake, *J. Geophys. Res.*, **108**(B1), 2012, doi:10.1029/2001JB000678.
- Kilb, D., and J. L. Hardebeck (2006), Fault parameter constraint using relocated earthquakes: A validation of first-motion focal-mechanism data, *Bull. Seismol. Soc. Am.*, **3**, 1140–1158, doi:10.1785/0120040239.
- Kisslinger, C. (1980), Evaluation of S to P amplitude ratios for determining focal mechanisms from regional network observations, *Bull. Seismol. Soc. Am.*, **70**(4), 999–1014.
- Kisslinger, C., J. Bowman, and K. Kock (1981), Procedures for computing focal mechanisms from local (SV/P)₂ data, *Bull. Seismol. Soc. Am.*, **71**(6), 1719–1729.
- Langston, C. A. (1981), Source inversion of seismic waveforms: The Koyna, India, earthquakes of 13 September 1967, *Bull. Seismol. Soc. Am.*, **71**(1), 1–24.
- Marcinkovich, C., and K. Olsen (2003), On the implementation of perfectly matched layers in a three-dimensional fourth-order velocity-stress finite difference scheme, *J. Geophys. Res.*, **108**(B5), 2276, doi:10.1029/2002JB002235.
- Margerin, L., M. Campillo, N. M. Shapiro, and B. Van Tiggelen (1999), Residence time of diffuse waves in the crust as a physical interpretation of coda Q: Application to seismograms recorded in Mexico, *Geophys. J. Int.*, **138**, 343–352.
- Margerin, L., M. Campillo, and B. Van Tiggelen (2000), Monte Carlo simulation of multiple scattering of elastic waves, *J. Geophys. Res.*, **105**(B4), 7873–7892.
- Marson-Pidgeon, K., B. L. N. Kennett, and M. Sambridge (2000), Source depth and mechanism inversion at teleseismic distances using a neighbourhood algorithm, *Bull. Seismol. Soc. Am.*, **90**(6), 1369–1383.
- Nakamura, M. (2002), Determination of focal mechanism solution using initial motion polarity of P and S waves, *Phys. Earth Planet. Inter.*, **130**, 17–29.
- Olsen, K. B. (1994), Simulation of three-dimensional wave propagation in the salt lake basin, Ph.D. thesis, Univ. of Utah, Salt Lake City, Utah.

- Olsen, K. B., A. Akinci, A. Rovelli, F. Marra, and L. Malagini (2006), 3D ground-motion estimation in Rome, Italy, *Bull. Seismol. Soc. Am.*, **96**(1), 133–146.
- Oppenheimer, D. H., P. A. Reasenberg, and R. W. Simpson (1988), Fault plane solutions for the 1984 Morgan Hill, California, earthquake sequence: Evidence for the state of stress on the Calaveras Fault, *J. Geophys. Res.*, **93**(B8), 9007–9026.
- Örgülü, G., M. Aktar, N. Türkelli, E. Sandvol, and M. Barazangi (2003), Contribution to the seismotectonics of Eastern Turkey from moderate and small size events, *Geophys. Res. Lett.*, **30**(24), 8040, doi:10.1029/2003GL018258.
- Pasyanos, M. E., D. S. Dreger, and B. Romanowicz (1996), Toward real-time estimation of regional moment tensors, *Bull. Seismol. Soc. Am.*, **86**(5), 1255–1269.
- Poupinet, G., W. L. Ellsworth, and J. Frechet (1984), Monitoring velocity variations in the crust using earthquake doublets: An application to the Calaveras Fault, California, *J. Geophys. Res.*, **89**(B7), 5719–5731.
- Pujol, J. (2003), *Elastic wave propagation and generation in seismology*, Cambridge Univ. Press, UK.
- Ramos-Martínez, J., and G. A. McMechan (2001), Source-parameter estimation by full waveform inversion in 3D heterogeneous, viscoelastic, anisotropic media, *Bull. Seismol. Soc. Am.*, **91**(2), 276–291.
- Randall, G. E., C. J. Ammon, and T. J. Owens (1995), Moment tensor estimation using regional seismograms from a Tibetan Plateau portable network deployment, *Geophys. Res. Lett.*, **22**(13), 1665–1668.
- Ratdomopurbo, A., and G. Poupinet (1995), Monitoring a temporal change of seismic velocity in a volcano: Application to the 1992 eruption of Mt. Merapi (Indonesia), *Geophys. Res. Lett.*, **22**(7), 775–778.
- Roberts, P. M., W. Scott Phillips, and M. C. Fehler (1992), Development of the active doublet method for measuring small velocity and attenuation changes in solids, *J. Acoust. Soc. Am.*, 3291–3302.
- Robinson, D., M. Sambridge, and R. Snieder (2007), Constraints on coda wave interferometry estimates of source separation: The acoustic case, *Exploration Geophysics*, **38**(3), 189–199.
- Saikia, C. K., and R. B. Hermann (1985), Application of waveform modeling to determine focal mechanisms of four 1982 Miramichi aftershocks, *Bull. Seismol. Soc. Am.*, **75**(4), 1021–1040.
- Scholz, C. H. (2004), *The mechanics of earthquakes and faulting*, 2nd ed., Cambridge Univ. Press.
- Shomali, Z. H., and R. Slunga (2000), Body wave moment tensor inversion of local earthquakes: An application to the South Iceland Seismic Zone, *Geophys. J. Int.*, **140**, 63–70.
- Sipkin, S. A. (1994), Rapid determination of global moment-tensor solutions, *Geophys. Res. Lett.*, **21**(16), 1667–1670.
- Snieder, R. (1999), Imaging and averaging in complex media, in *Diffuse waves in complex media*, NATO Science Series C, vol. 531, edited by J. P. Fouque, pp. 405–454, Kluwer Academic Publishers.
- Snieder, R. (2004), Extracting the Green's function from the correlation of coda waves: A derivation based on stationary phase, *Phys. Rev. E*, **69**, 046,610.
- Snieder, R. (2006), The theory of coda wave interferometry, *Pure Appl. Geophys.*, **163**, 455–473.
- Snieder, R., and M. Vrijlandt (2005), Constraining the source separation with coda wave interferometry: Theory and application to earthquake doublets in the Hayward Fault, California, *J. Geophys. Res.*, **110**, B04301, doi:10.1029/2004JB003317.
- Snieder, R., A. Grêt, H. Douma, and J. Scales (2002), Coda wave interferometry for estimating nonlinear behaviour in seismic velocity, *Science*, **295**, 2253–2255, doi:10.1126/science.1070015.
- Snoke, A. (2003), FOCMEC: FOCal MECHANism determinations, in *International Handbook of Earthquake and Engineering Seismology: Part B*, edited by W. H. K. Lee, H. Kanamori, P. C. Jennings, and C. Kisslinger, chap. 85.12, pp. 1629–1630, Academic Press.
- Stein, S., and M. Wyssession (2003), *An introduction to seismology, earthquakes, and earth structure*, Blackwell Publishing.
- Stein, S., and M. Wyssession (2004), *An introduction to seismology. earthquakes, and Earth structure*, Blackwell Publishing, USA.
- Sykes, L. R. (1967), Mechanism of earthquakes and nature of faulting on the mid-oceanic ridges, *J. Geophys. Res.*, **72**(8), 2131–2153.
- Thurber, C., H. Zhang, F. Waldhauser, J. Hardebeck, A. Michael, and D. Eberhart-Phillips (2006), Three-dimensional compressional wave-speed model, earthquake relocations, and focal mechanisms for the Parkfield, California, Region, *Bull. Seismol. Soc. Am.*, **96**(4B), S38–S49, doi:10.1785/0120050825.
- Zhao, L.-S., and D. V. Helmberger (1994), Source estimation from broadband regional seismograms, *Bull. Seismol. Soc. Am.*, **84**(1), 91–104.

D. J. Robinson and M. Sambridge, Research School of Earth Sciences, Australian National University, Canberra, ACT, 0200, Australia. (david.robinson@anu.edu.au; malcolm.sambridge@anu.edu.au)

R. Snieder, Center for Wave Phenomena and Department of Geophysics, Colorado School of Mines, Golden, CO 80401, USA. (rsnieder@mines.edu)